JACS
JOURNAL OF THE AMERICAN CHEMICAL SOCIETY
Article
pubs.acs.org/JACS

Single Gold@Silver Nanoprobes for Real-Time Tracing the Entire Autophagy Process at Single-Cell Level

Zixuan Chen,[†,§] Jingjing Li,[‡,§] Xueqin Chen,[†] Juntao Cao,[†] Jianrong Zhang,[†] Qianhao Min,*[,†] and Jun-Jie Zhu*[,†]

[†]State Key Laboratory of Analytical Chemistry for Life Science, School of Chemistry and Chemical Engineering, Synergetic Innovation Center of Chemistry for Life Science, Nanjing University, Nanjing 210093, PR China

[‡]School of Medical Imaging, Xuzhou Medical College, Xuzhou 221004, PR China

Supporting Information

ABSTRACT: This article describes a multimodified core−shell gold@silver nanoprobe for real-time monitoring the entire autophagy process at single-cell level. Autophagy is vital for understanding the mechanisms of human pathologies, developing novel drugs, and exploring approaches for autophagy controlling. A major challenge for autophagy study lies in real-time monitoring. One solution might come from real-time detection of in situ superoxide radicals ($O_2^{\bullet-}$), because it is the main regulator of autophagy. In this work, our proposed nanoprobes were etched by $O_2^{\bullet-}$ and gave a notable wavelength change in the plasmon resonance scattering spectra. Both the experimental and simulated results suggested the wavelength change rate correlated well with $O_2^{\bullet-}$ level. This response enabled its application in real-time in situ quantification of $O_2^{\bullet-}$ during autophagy course. More importantly, with the introduction of "relay probe" operation, two types of $O_2^{\bullet-}$-regulating autophagy processes were successfully traced from the beginning to the end, and the possible mechanism was also proposed.

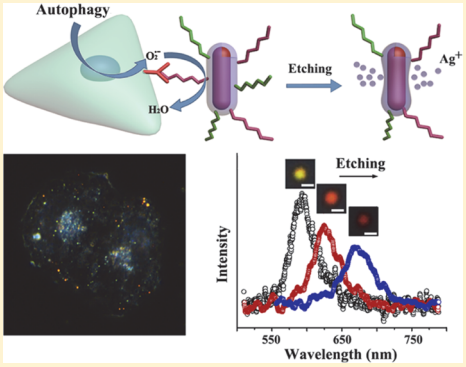

INTRODUCTION

Autophagy is a regulated lysosomal degradation pathway along with the formation of double vacuoles, called autophagosomes.[1,2] It serves as a survival mechanism to maintain nutrient and energy levels during periods of metabolic starvation or stress.[3−6] The enclosed organelles are then degraded to produce essential amino acids and fatty acids, which are used to synthesize protein or are oxidized by mitochondrial electron transport chain (mETC) to generate ATP for cell survival.[7,8] Autophagy is involved in a great variety of functions, such as cell growth, survival, and death.[9] Therefore, real-time tracing of the entire autophagy process is vital for further understanding the mechanisms of human pathologies, developing novel drugs and exploring approaches for autophagy controlling.[2,10] Unfortunately, present methods for autophagy detection, including Western blot analysis and GFP-Atg8/LC3 fluorescence method, are far from the requirement of real-time and long-term monitoring.[9] Autophagy is mainly regulated by mitochondrial reactive oxygen species (ROS), especially superoxide radicals ($O_2^{\bullet-}$).[11,12] When cells were under starvation condition, the mitochondria mediated oxidative phosphorylation became incomplete, and the production of $O_2^{\bullet-}$ was upregulated, which induced the autophagy.[13] Thus, real-time intracellular $O_2^{\bullet-}$ level can trace autophagy effectively. Current methods for $O_2^{\bullet-}$ detection, such as electron spin resonance (ESR),[14] electrochemistry,[15,16] were usually ruinous and not suitable for live cells observation. Methods for long-term and real-time detection of $O_2^{\bullet-}$ at single-cell level are still deficient.

Herein, we report a plasmon resonance scattering (PRS) nanoprobe-based approach for real-time monitoring the intracellular $O_2^{\bullet-}$ level. This design was realized by notable PRS spectral shift $\Delta\lambda_{max}$ of nanoprobe when the silver shell was etched by the generated $O_2^{\bullet-}$. Noble metal nanoparticles have been widely used as PRS nanoprobes in the field of cellular imaging and biosensing in recent years.[17−23] Their negligible photobleaching and single molecule intensity fluctuations (i.e., blinking) provide excellent optical stability.[24] Additionally, PRS intensity from single noble metal nanoparticle was much stronger than the fluorescent emissions from a typical chromophore or a quantum dot,[25] which favored their applications at single-particle level and achievement of a lower detection limit owing to its effective detection volume.[26] Moreover, extraordinary chemical stability, low toxicity and excellent biocompatibility of noble metal nanoparticles are fit for cellular and *in vivo* imaging.[27]

RESULTS AND DISCUSSION

To fabricate a stable and specific targeting PRS nanoprobe, polyethylene glycol (PEG) and Arg-Gly-Asp-Cys (RGD) peptides were conjugated on the surface of Au@Ag nanorods

Received: November 3, 2014
Published: January 21, 2015

DOI: 10.1021/ja5112628
J. Am. Chem. Soc. 2015, 137, 1903−1908

(Figure 1a). This nanoprobe could be specifically captured by cancer cells through the targeted binding interactions between

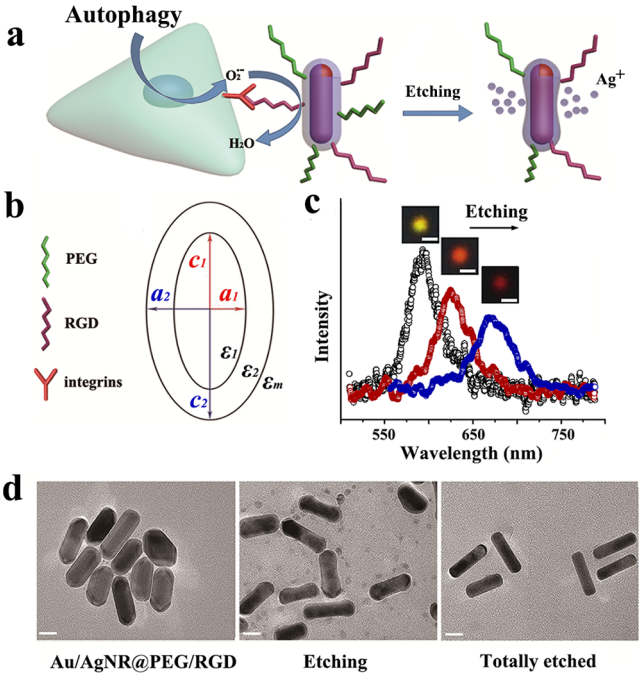

Figure 1. (a) Illustration of the core–shell structure Au@AgNRs. (b) The model controlling PRS spectrum of Au@AgNRs, where the prolate spheroidal dielectric (ε_1) core, with semiaxes $a_1 < c_1$, is coated with another confocal spheroidal dielectric (ε_2) shell with semiaxes $a_2 < c_2$. ε_m is the dielectric functions of adjacent medium. (c) PRS spectra of a single probe etched by $O_2^{\bullet-}$ for 0, 30, and 60 min. Insets showed scattering images of the probe in each status. Scale bar was 500 nm. (d) HRTEM micrograph illustrated the transitions of nanoprobes during the etching process. Scale bar was 20 nm.

RGD peptides and integrins ($\alpha v\beta 3$ or $\alpha v\beta 5$) on the membrane. When exposed to $O_2^{\bullet-}$, silver shell of the nanoprobe was easily etched to Ag^+ and then diffused into bulk solution. PRS λ_{max} was determined by the aspect ratio of gold@silver nanorod based on Mie scattering theory (Figure 1b).[28,29] Because the etching reaction preferentially occurred on the side of the nanorods based on its higher surface energy,[30] the formed bone-shaped nanoprobes gave rise to an increased aspect ratio (c_2/a_2), and a notable $\Delta\lambda_{max}$.

This $O_2^{\bullet-}$-induced $\Delta\lambda_{max}$ were systematically investigated in the presence of 200 mU mL^{-1} xanthine oxidase (XOD) and 100 μM hypoxanthine (HX), which generated a stable 2 μM $O_2^{\bullet-}$.[31] After treated by $O_2^{\bullet-}$, λ_{max} of a single nanoprobe was observed shifting from 580 to 675 nm, along with a decreasing scattering intensity (Figure 1c). Scattering light color also changed from yellow to red simultaneously. Such a proposed reaction mechanism was testified by the HRTEM images (Figure 1d). Nanoprobes without any treatment presented an intact core–shell structure. After treated by $O_2^{\bullet-}$ for 30 min, a noticeable collapse appeared on the side of nanoprobes, leading to the formation of bone-shaped nanorods. Silver shell was totally etched after 1 h treatment and uniform gaps between gold nanorods was observed, attributed to the dissolved silver shell.

To obtain the best sensitivity, aspect ratio (c_1/a_1) of nanoprobes was optimized by kinetic model simulation (Figure S1, Supporting Information). Spectral red-shift rate of nanoprobes with different aspect ratio was simulated based on the proposed model (Figure 1b).[28,29] Longer aspect ratio gave higher red-shift rate. Because the spectrum CCD got most effective absorption between 500 and 700 nm, nanoprobes with ~600 nm original PRS wavelength was selected for the subsequent experiments. Size-dependent red-shift rate of the nanoprobes was also simulated (Figure S2). Smaller size presented higher red-shift rate. However, considering the efficiency of scattering scales down with a_1^6, we finally selected the smallest nanoprobes (a_1 = 6.5 nm). In this size, we could still observe it clearly by DFM.

Because the detection mechanism of this nanoprobe is the etching of silver shell, excess coverage of biomolecules can block the active sites. To investigate the effect of RGD coverage level to the $O_2^{\bullet-}$ sensitivity, Au@Ag nanorods were modified by RGD with different coverage level through tuning the molar ratio between RGD and nanorods. Figure 2a displayed 6 normalized UV–vis spectra of nanoprobes modified with

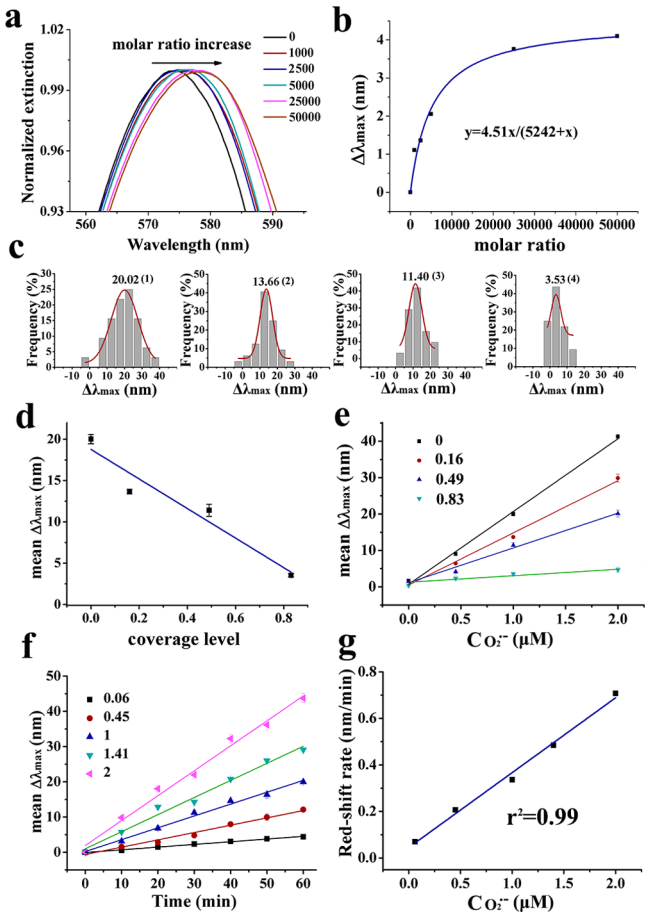

Figure 2. (a) Normalized UV–vis spectra of Au@AgNRs modified by RGD peptide at different molar ratio (RGD: nanorods). (b) $\Delta\lambda_{max}$ of UV–vis spectra vs nanoprobes modified by 0 molar RGD. Insets illustrated the fitting curve equation. (c) $\Delta\lambda_{max}$ distributions of Au@AgNRs modified with 0 (1), 0.16 (2), 0.49 (3) and 0.83 (4) coverage level of RGD when exposed to 1 μM $O_2^{\bullet-}$ for 30 min. (d) Mean value of $\Delta\lambda_{max}$ distributions (black dots) and calculated result (blue curve) at different coverage levels. (e) Mean $\Delta\lambda_{max}$ of all nanorods upon treatment with 0, 0.45, 1, and 2 μM $O_2^{\bullet-}$. (f) Time-dependent mean $\Delta\lambda_{max}$ of probes upon treatment with 0.06, 0.45, 1, 1.41, and 2 μM $O_2^{\bullet-}$. (g) Calibration plot corresponding to the red-shift rate with the $O_2^{\bullet-}$ concentration.

DOI: 10.1021/ja5112628
J. Am. Chem. Soc. 2015, 137, 1903–1908

different molar ratios. These spectra showed varied $\Delta\lambda_{max}$ to the molar ratio, which was attributed to the higher refractive index of RGD (~1.65) than the adjacent medium (~1.33). $\Delta\lambda_{max}$ at different molar ratios fitted a typical saturation binding curve (Figure 2b). According to eq S4, the maximum $\Delta\lambda_{max}$ was evaluated to be 4.51 nm and K_d (molar ratio to achieve a half-maximum binding) was 5242. The coverage level f, ranging from 0 to 1, at different molar ratio was also evaluated by eq S2.

Nanoprobes with different coverage level were then incubated in 1 μM $O_2^{\bullet-}$ for 30 min to investigate the RGD coverage effect on $O_2^{\bullet-}$ sensitivity. By recording the spectra of 30 randomly nanoprobes before and after 30 min incubation, a group of Gaussian-shaped distributions of $\Delta\lambda_{max}$ was obtained (Figure 2c). The width of distributions in the same condition might be caused by the tiny deviations in the morphology, core size and shell thickness among the individual core−shell rods, as well as the small deviations in the coverage levels of their ligants and the ratio between two ligands of the rods. Mean values of $\Delta\lambda_{max}$ distributions and coverage level were plotted in Figure 2d. Increasing coverage level resulted in a linear decreased mean $\Delta\lambda_{max}$, revealing that the sensitivity to $O_2^{\bullet-}$ was affected by RGD coverage level.

$\Delta\lambda_{max}$ response of nanoprobes with different RGD coverage level to $O_2^{\bullet-}$ concentrations were investigated (Figure 2e). $\Delta\lambda_{max}$ of all nanoprobes scaled up linearly with $O_2^{\bullet-}$ concentration and the slopes reduced with the RGD coverage level increase. In this case, the RGD coverage should be controlled at the lowest level for larger $\Delta\lambda_{max}$. But the target performance to integrins on cell membrane should be concerned also. For this aim, HeLa cells were treated by 0.04 nM nanoprobes with different RGD coverage levels for 30 min to examine the target ability (Figure S3). Cells treated with 0.32 coverage level RGD showed only few scattering dots on the membrane. But once the RGD coverage level grew over 0.49, nanoprobes displayed good target performance to the cells. Considering these experimental results, 0.49 was selected as the RGD coverage level finally.

In Figure 2e, we learned that the mean $\Delta\lambda_{max}$ of proposed nanoprobes in 30 min was linear with $O_2^{\bullet-}$ concentration, but the kinetic spectral red-shift rate was still not clear. To address this, optimized nanoprobes were incubated in series concentrations of $O_2^{\bullet-}$ for 60 min, ranging from 60 nM to 2 μM. PRS spectra of randomly selected 30 single nanoprobes were acquired in the interval of 10 min to obtain kinetic $\Delta\lambda_{max}$. Figure S7 illustrated all the Gaussian-shaped distributed $\Delta\lambda_{max}$ of these nanoprobes. The real-time mean $\Delta\lambda_{max}$ was plotted in Figure 2f, and a group of time-dependent $\Delta\lambda_{max}$ shift curves were fitted. These linear curves revealed that the $\Delta\lambda_{max}$ increased linearly with the response time and the red-shift rates were determined by $O_2^{\bullet-}$ concentrations. The real-time spectral red-shift rates at different $O_2^{\bullet-}$ concentrations were evaluated from the slopes of those time-dependent $\Delta\lambda_{max}$ curves (Figure 2g) and they scaled up with $O_2^{\bullet-}$ concentrations from 60 nM to 2 μM, providing the possibility of real-time $O_2^{\bullet-}$ monitoring. These experimental results were supported by kinetics models (eq S7). High sensitivity and remarkable linear response of proposed nanoprobes to $O_2^{\bullet-}$ revealed the potential in real-time cellular $O_2^{\bullet-}$ analysis.

To apply the proposed nanoprobes for monitoring $O_2^{\bullet-}$-regulated autophagy in live cells, its stability should be first evaluated when exposed to acid, base and hydroperoxide (H_2O_2). Amazingly, PRS λ_{max} of nanoprobes showed response to neither pH changes nor H_2O_2 (Figure S4, S5), revealing its outstanding stability. Cytotoxicity is another important factor on concern for foreign materials in living system. With MTT assay, HeLa cells displayed more than 91% viabilities even after 72 h incubation with 0.04 nM of nanoprobes (Figure S6). The specific binding ability of the nanoprobes to target HeLa cells was also evaluated using MCF-7 adenocarcinoma cells as control. MCF-7 was reported to express significant low integrin on the membrane.[32] Figure 3a,b demonstrated dark-field

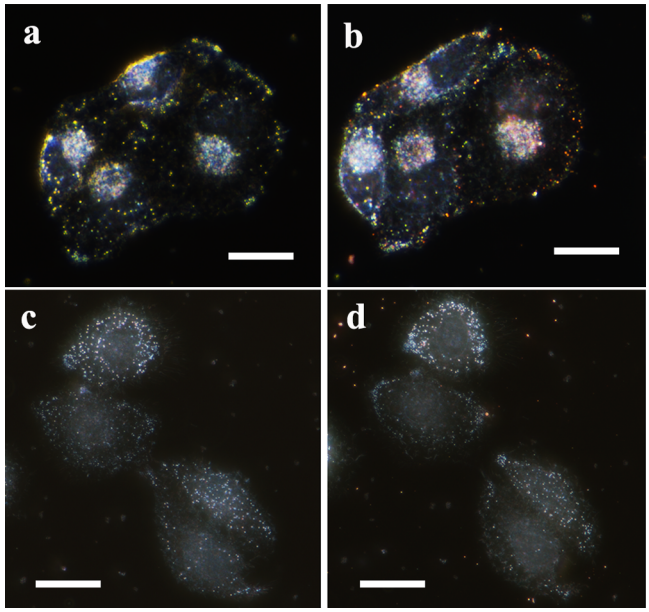

Figure 3. Representative DFM images of HeLa cells with (a) and without (b) nanoprobes treatment. Representative DFM images of MCF-7 cells with (c) and without (d) nanoprobes treatment. Both cells were both cultured with 0.04 nM probe for 30 min. Scale bar was 20 μm.

images of HeLa cells before and after treated by 0.04 nM nanoprobes for 30 min, and abundant orange scattering dots were presented on the membrane (Figure 3b). On the contrary, MCF-7 cells displayed only rare scattering dots (Figure 3c,d), indicating the excellent specificity of the nanoprobes.

Autophagy monitoring was then performed with our proposed nanoprobes. HeLa cells were treated by GP-starvation medium (glucose, L-glutamine, pyruvate, and serum) for 1 h to induce the autophagy and then incubated with nanoprobes.[10,13] As shown in Figure 4a, several orange scattering light spots were presented on a single HeLa cell membrane, corresponding to the captured nanoprobes. After 2 h, the orange scattering light spots turned red and the scattering light brightness decreased (Figure 4b). Scattering spectra of 3 captured nanoprobes were also displayed (Figure 4c−e), notable spectral red-shift $\Delta\lambda_{max}$ was observed within 2 h, indicating the rising $O_2^{\bullet-}$ level. HeLa cells under normal condition were incubated with nanoprobes for 2 h as control. In stark contrast, no obvious color change except a little brightness decrease was observed in control group (Figure 4f,g). Scattering spectra (Figure 4h−j) also suggested that $\Delta\lambda_{max}$ in GP-starvation group were resulted from the $O_2^{\bullet-}$ generated under starvation treatment.

To evaluate the $O_2^{\bullet-}$ concentration, $\Delta\lambda_{max}$ distributions of 30 selected nanoprobes captured by HeLa cells under GP-starvation and normal condition were acquired respectively (Figure 5). The mean value of $\Delta\lambda_{max}$ distributions under GP-

DOI: 10.1021/ja5112628
J. Am. Chem. Soc. 2015, 137, 1903−1908

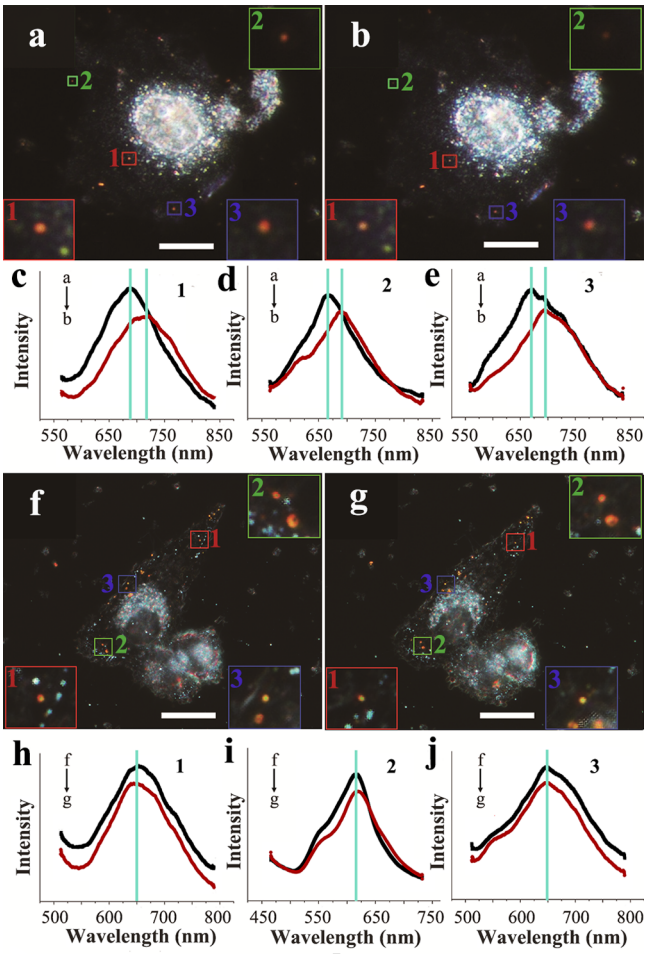

Figure 4. (a) DFM images showed one HeLa cell under 1 h of GP-starvation with individual probes captured on the membrane. Insets showed the detailed view of 3 individual probes numbered with 1–3. (b) DFM images showed the same cell in (a) after another 2 h of starvation duration. Insets showed the detailed view of 3 corresponding probes in (a). Scale bar was 10 μm. (c–e) Scattering spectra changes of 3 probes between (a) and (b). (f) DFM images showed another HeLa cell in normal condition with individual probes captured on the membrane. Insets showed the detailed view of 3 individual probes numbered with 1–3. (g) DFM images showed the same HeLa cell in (f) after 2 h culture. Insets showed the detailed view of 3 corresponding probes in (f). Scale bar was 10 μm. (h–j) Scattering spectra changes of 3 probes between (f) and (g).

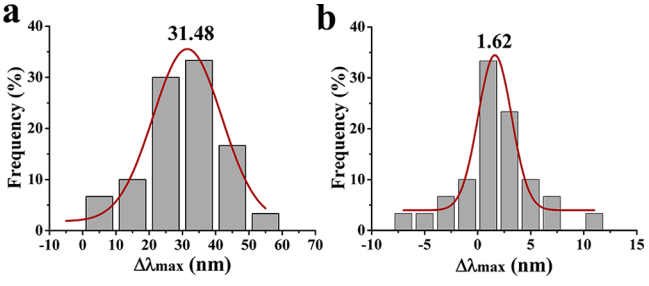

Figure 5. $\Delta\lambda_{max}$ distributions of nanoprobes captured by HeLa cells under GP-starvation (a) and normal condition (b) for 2 h.

starvation within 2 h was 31.48 nm (Figure 5a), and $O_2^{\bullet-}$ concentration was evaluated to be ~0.67 μM according to the calibration result (Figure 2g). In contrast, the mean value of $\Delta\lambda_{max}$ distributions under normal condition was only 1.62 nm (Figure 5b), which might be caused by the nonspecific adsorption of biomolecules.

To further investigate how $O_2^{\bullet-}$ level regulates the autophagy process, HeLa cells were incubated with nanoprobes and acridine orange simultaneously. The acridine orange was used to stain the acidic vesicular organelles (AVOs). While autophagy occurs, double-membrane vesicles, termed autophagosomes, encloses organelles and fuses with lysosome to form autolysosomes, which is a type of AVOs. These AVOs are then degraded to produce essential amino acids and fatty acids, which are used to synthesize protein or are oxidized by mETC to generate ATP for cell survival.[8,9] Fluorescence images of HeLa cells during an entire GP-starvation process were presented (Figure S8a). Red puncta dots (AVOs) were not observed until cells were starved for 6 h. The maximal amount of AVOs was observed when starved for 36 h. Quantified result (Figure S8b) was evaluated from the mean fluorescence intensity of puncta dots in at least 50 cells in each period of autophagy and the generation rate of autolysosomes was herein calculated (Figure S8c). Once the autophagy was induced by starvation, the generation rate of autolysosomes increased rapidly and then kept steady for 36 h. Surprisingly, the autolysosome generation rate fitted the evolution trend of $O_2^{\bullet-}$ level extremely well, confirming the feasibility of $O_2^{\bullet-}$-based autophagy monitoring.

To eventually achieve the entire autophagy tracing of single cells, which commonly lasted few days, long-term valid nanoprobes are necessary. Most of reported nanoprobes, especially those with high sensitivity, cannot keep sensitive to objects for such a long period because reaction is usually irreversible. During an entire autophagy process, nanoprobes could be invalid and scattering light brightness became too low to be detected. To solve this issue, a unique operation, called "relay probe", was proposed here (Scheme 1). Cells cultured in

Scheme 1. Relay Probe Operation Procedure

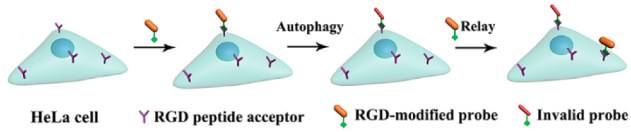

normal medium captured the nanoprobes rapidly by RGD acceptor on the cell membrane.[33] After rinsed, cells were treated by starvation medium to induce autophagy, and $\Delta\lambda_{max}$ of captured nanoprobes were recorded. Once these nanoprobes were invalid, fresh nanoprobes was introduced and worked instead. That was a "relay" of nanoprobes. Relays of following nanoprobes were performed by the same way. This relay probe operation was repeated until no $\Delta\lambda_{max}$ could be detected any more. Because nanoprobes kept a constant sensitivity all the time and cells were always in autophagy process, real-time $O_2^{\bullet-}$ level in target cells could be monitored during the entire autophagy process.

To evaluate the feasibility of our design, this relay probe operation was used to observe the autophagy of a single HeLa cell under GP-starvation. Representative DFM images indicated that cell kept normal within 6 h (Figure 6a,b). After starvation for 20 h, autophagy was displayed due to visible cell shrinkage (Figure 6c). In the residual period, no more morphological change was witnessed (Figure 6d,e). Several batches of captured nanoprobes were clearly observed on the cell membrane even the cell shrank. After 55 h starvation treatment,

DOI: 10.1021/ja5112628
J. Am. Chem. Soc. 2015, 137, 1903–1908

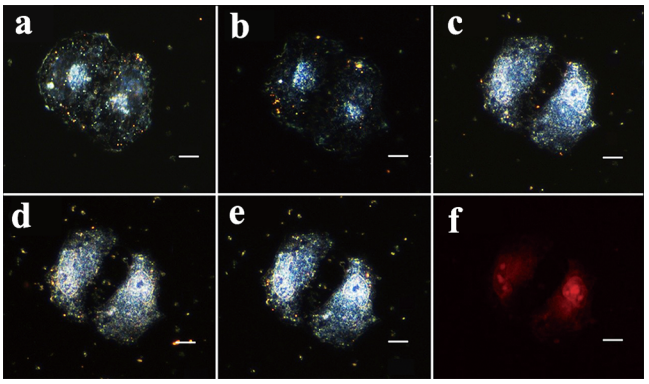

Figure 6. Representative DFM images of a HeLa cell treated by relay probe operation during an entire autophagy. The cell with several batches of probes was under GP-starvation condition for 0 h (a), 6 h (b), 20 h (c), 48 h (d) and 55 h (e). (f) Fluorescence micrographs of the cell in (e) stained by acridine orange. Scale bar was 10 μm.

nanoprobes stopped changing, indicating the ending of autophagy. To confirm, the cell was stained by acridine orange (Figure 6f). Rare puncta dots revealed the exhaust of autolysosomes, which was the signal of the termination of autophagy.

Relay probe operation was then used for real-time tracing the entire autophagy process of HeLa cells under GP-starvation. During this process, eight batches of probes were introduced. In Figure 7a, 8 groups of time-continuous $\Delta\lambda_{max}$ were obtained from the statistical data in different cells. According to the time-dependent $\Delta\lambda_{max}$ variation rates, the real-time in situ $O_2^{\bullet-}$ level was evaluated (Figure 7b). The $O_2^{\bullet-}$ concentration increased rapidly after the introduction of starvation medium. It kept steady at the maximum for a long period and finally fell down. We have investigated the relationship between autolysosome

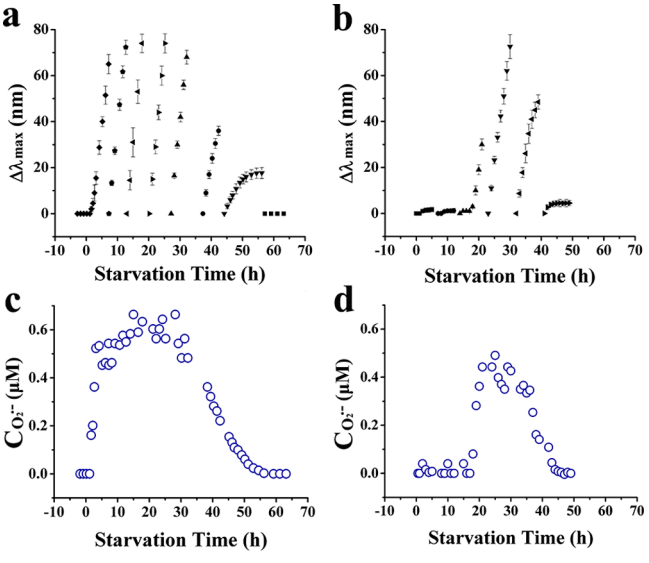

Figure 7. (a) Time-dependent mean $\Delta\lambda_{max}$ of several successive batches of nanoprobes on HeLa cells during the entire autophagy process induced by GP-starvation. (b) Calculated time-dependent $O_2^{\bullet-}$ concentration in HeLa cells under GP-starvation. (c) Time-dependent mean $\Delta\lambda_{max}$ of several successive batches of nanoprobes on HeLa cells during the entire autophagy process induced by AA-starvation. (d) Calculated time-dependent $O_2^{\bullet-}$ concentration in HeLa cells under AA-starvation.

generation rate and $O_2^{\bullet-}$ level (Figure S8). Since the generation rate of autolysosome showed some correlation with the $O_2^{\bullet-}$ concentration, the entire autophagy process of the target cell was proposed. Before starvation, low $O_2^{\bullet-}$ level suggested no autophagy occurred. Once autophagy was induced by GP-starvation, $O_2^{\bullet-}$ concentration increased quickly. During this period, cells began to produce autolysosomes to degrade the organelles and generate ATP for survival. When the generated ATP was sufficient, $O_2^{\bullet-}$ concentration stopped increasing to provide a steady amount of autolysosomes. Once most of the organelles were degraded, including the mitochondria, the production of $O_2^{\bullet-}$ from mETC was hampered by the lack of organelles.[13,34,35] As a result, $O_2^{\bullet-}$ concentration decreased, followed by the deceleration and termination of autolysosomes generation. Once the residual autolysosomes self-degraded, the autophagy was ended.

The autophagy process of HeLa cells under AA-starvation (amino acids and serum) was also studied for comparison (Figure 7c,d). The $O_2^{\bullet-}$ concentration of HeLa cells under AA-starvation showed a similar trend as the GP-starvation, except some timing dissimilarities. When AA-starvation medium was introduced, the $O_2^{\bullet-}$ concentration did not show noticeable change until 15 h later and reached maximal after more than 20 h. In addition, the steady duration was only several hours, which was much shorter than GP-starvation (>20 h). These differences might come from the different inducing mechanisms. Autophagy under GP-starvation was chiefly induced by the up-regulated $O_2^{\bullet-}$ level. However, in the case of AA-starvation, H_2O_2 was initially increased, leading to the subsequent increase of $O_2^{\bullet-}$ level and then autophagy eventually.[10] Thus, $O_2^{\bullet-}$ concentration increase in HeLa cells under AA-starvation condition was much slower.

CONCLUSION

In conclusion, entire autophagy of single HeLa cells was real-time traced by multifunctionalized core–shell gold@silver nanoprobes. The nanoprobes showed high sensitivity to $O_2^{\bullet-}$ concentration by visible PRS red-shift. In addition, it exhibit a good specific target to cells with integrin on the membrane. To our knowledge, it is the first report for real-time tracing entire autophagy at single-cell level. According to our results, intracellular $O_2^{\bullet-}$ level controlled the autophagy process by mediating the autolysosome generation. Different starvation approaches can induce different autophagy processes, such as diverse steady state time-consuming. Concerning the key role of autophagy in the witness of cytometaplasia, our proposed method owns the potentials in studying the mechanisms of human pathologies, developing novel drugs or exploring approaches for controlling autophagy in human diseases.

ASSOCIATED CONTENT

Supporting Information

Full experimental procedures and additional supplementary figures. This material is available free of charge via the Internet at http://pubs.acs.org.

AUTHOR INFORMATION

Corresponding Authors

minqianhao@nju.edu.cn
jjzhu@nju.edu.cn

DOI: 10.1021/ja5112628
J. Am. Chem. Soc. 2015, 137, 1903–1908

Author Contributions

[§]Z.C. and J.L. contributed equally.

Notes

The authors declare no competing financial interest.

■ ACKNOWLEDGMENTS

This research was supported by the National Basic Research Program of China (2011CB933502), National Natural Science Foundation of China (21335004, 21205060, and 21427807).

■ REFERENCES

(1) Levine, B.; Yuan, J. Y. *J. Clin. Invest.* **2005**, *115*, 2679−2688.
(2) He, C. C.; Klionsky, D. J. *Regulation Mechanisms and Signaling Pathways of Autophagy*; Annual Reviews: Palo Alto, 2009; Vol. *43*, pp 67−93.
(3) Foote, C. S. *Acc. Chem. Res.* **1968**, *1*, 104−110.
(4) Scherz-Shouval, R.; Elazar, Z. *Trends Biochem. Sci.* **2011**, *36*, 30−38.
(5) Scherz-Shouval, R.; Elazar, Z. *Trends Cell Biol.* **2007**, *17*, 422−427.
(6) Danial, N. N.; Korsmeyer, S. J. *Cell* **2004**, *116*, 205−219.
(7) Klionsky, D. J.; Abeliovich, H.; Agostinis, P.; Agrawal, D. K.; Aliev, G.; Askew, D. S.; Baba, M.; Baehrecke, E. H.; Bahr, B. A.; Ballabio, A.; Bamber, B. A.; Bassham, D. C.; Bergamini, E.; Bi, X. N.; Biard-Piechaczyk, M.; Blum, J. S.; Breclesen, D. E.; Brodsky, J. L.; Brumell, J. H.; Brunk, U. T.; Bursch, W.; Camougrand, N.; Cebollero, E.; Cecconi, F.; Chen, Y. Y.; Chin, L. S.; Choi, A.; Chu, C. T.; Chung, J. K.; Clarke, P. G. H.; Clark, R. S. B.; Clarke, S. G.; Clave, C.; Cleveland, J. L.; Codogno, P.; Colombo, M. I.; Coto-Montes, A.; Cregg, J. M.; Cuervo, A. M.; Debnath, J.; Demarchi, F.; Dennis, P. B.; Dennis, P. A.; Deretic, V.; Devenish, R. J.; Di Sano, F.; Dice, J. F.; DiFiglia, M.; Dinesh-Kumar, S.; Distelhorst, C. W.; Djavaheri-Mergny, M.; Dorsey, F. C.; Droge, W.; Dron, M.; Dunn, W. A.; Duszenko, M.; Eissa, N. T.; Elazar, Z.; Esclatine, A.; Eskelinen, E. L.; Fesues, L.; Finley, K. D.; Fuentes, J. M.; Fueyo, J.; Fujisaki, K.; Galliot, B.; Gao, F. B.; Gewirtz, D. A.; Gibson, S. B.; Gohla, A.; Goldberg, A. L.; Gonzalez, R.; Gonzalez-Estevez, C.; Gorski, S.; Gottlieb, R. A.; Haussinger, D.; He, Y. W.; Heidenreich, K.; Hill, J. A.; Hoyer-Hansen, M.; Hu, X.; Huang, W. P.; Iwasaki, A.; Jaattela, M.; Jackson, W. T.; Jiang, X.; Jin, S. K.; Johansen, T.; Jung, J. U.; Kadowaki, M.; Kang, C.; Kelekar, A.; Kessel, D. H.; Kiel, J.; Kim, H. P.; Kimchi, A.; Kinsella, T. J.; Kiselyov, K.; Kitamoto, K.; Knecht, E.; Komatsu, M.; Kominami, E.; Konclo, S.; Kovacs, A. L.; Kroemer, G.; Kuan, C. Y.; Kumar, R.; Kundu, M.; Landry, J.; Laporte, M.; Le, W. D.; Lei, H. Y.; Lenardo, M. J.; Levine, B.; Lieberman, A.; Lim, K. L.; Lin, F. C.; Liou, W.; Liu, L. F.; Lopez-Berestein, G.; Lopez-Otin, C.; Lu, B.; Macleod, K. F.; Malorni, W.; Martinet, W.; Matsuoka, K.; Mautner, J.; Meijer, A. J.; Melendez, A.; Michels, P.; Miotto, G.; Mistiaen, W. P.; Mizushima, N.; Mograbi, B.; Monastyrska, I.; Moore, M. N.; Moreira, P. I.; Moriyasu, Y.; Motyl, T.; Munz, C.; Murphy, L. O.; Naqvi, N. I.; Neufeld, T. P.; Nishino, I.; Nixon, R. A.; Noda, T.; Nurnberg, B.; Ogawa, M.; Oleinick, N. L.; Olsen, L. J.; Ozpolat, B.; Paglin, S.; Palmer, G. E.; Papassideri, I.; Parkes, M.; Perlmutter, D. H.; Perry, G.; Piacentini, M.; Pinkas-Kramarski, R.; Prescott, M.; Proikas-Cezanne, T.; Raben, N.; Rami, A.; Reggiori, F.; Rohrer, B.; Rubinsztein, D. C.; Ryan, K. M.; Sadoshima, J.; Sakagami, H.; Sakai, Y.; Sandri, M.; Sasakawa, C.; Sass, M.; Schneider, C.; Seglen, P. O.; Seleverstov, O.; Settleman, J.; Shacka, J. J.; Shapiro, I. M.; Sibirny, A.; Silva-Zacarin, E. C. M.; Simon, H. U.; Simone, C.; Simonsen, A.; Smith, M. A.; Spanel-Borowski, K.; Srinivas, V.; Steeves, M.; Stenmark, H.; Stromhaug, P. E.; Subauste, C. S.; Sugimoto, S.; Sulzer, D.; Suzuki, T.; Swanson, M. S.; Takeshita, F.; Talbot, N. J.; Talloczy, Z.; Tanaka, K.; Tanaka, K.; Tanida, I.; Taylor, G. S.; Taylor, J. P.; Terman, A.; Tettamanti, G.; Thompson, C. B.; Thumm, M.; Tolkovsky, A. M.; Tooze, S. A.; Truant, R.; Tumanovska, L. V.; Uchiyama, Y.; Ueno, T.; Uzcategui, N. L.; van der Klei, I.; Vaquero, E. C.; Vellai, T.; Vogel, M. W.; Wang, H. G.; Webster, P.; Wiley, J. W.; Xi, Z. J.; Xiao, G.; Yahalom, J.; Yang, J. M.; Yap, G.; Yin, X. M.; Yoshimori, T.; Yu, L.; Yue, Z. Y.; Yuzaki, M.; Zabirnyk, O.; Zheng, X. X.; Zhu, X.; Deter, R. L.; Tabas, I. *Autophagy* **2008**, *4*, 151−175.
(8) Jin, S.; White, E. *Autophagy* **2007**, *3*, 28−31.
(9) Mizushima, N.; Levine, B.; Cuervo, A. M.; Klionsky, D. J. *Nature* **2008**, *451*, 1069−75.
(10) Chen, Y.; Azad, M. B.; Gibson, S. B. *Cell Death Differ.* **2009**, *16*, 1040−52.
(11) Azad, M. B.; Chen, Y.; Gibson, S. B. *Antioxid. Redox Signaling* **2009**, *11*, 777−790.
(12) Moore, M. N. *Autophagy* **2008**, *4*, 254−256.
(13) Li, L.; Chen, Y.; Gibson, S. B. *Cell. Signalling* **2013**, *25*, 50−65.
(14) Deschacht, M.; Horemans, T.; Martinet, W.; Bult, H.; Maes, L.; Cos, P. *Free Radical Res.* **2010**, *44*, 763−772.
(15) Amatore, C.; Arbault, S.; Bouton, C.; Drapier, J.-C.; Ghandour, H.; Koh, A. C. W. *ChemBioChem* **2008**, *9*, 1472−1480.
(16) Wegerich, F.; Turano, P.; Allegrozzi, M.; Möhwald, H.; Lisdat, F. *Anal. Chem.* **2009**, *81*, 2976−2984.
(17) Zhang, L.; Li, Y.; Li, D.-W.; Jing, C.; Chen, X.; Lv, M.; Huang, Q.; Long, Y.-T.; Willner, I. *Angew. Chem., Int. Ed.* **2011**, *50*, 6789−6792.
(18) Kang, B.; Mackey, M. A.; El-Sayed, M. A. *J. Am. Chem. Soc.* **2010**, *132*, 1517−1519.
(19) Austin, L. A.; Kang, B.; Yen, C.-W.; El-Sayed, M. A. *J. Am. Chem. Soc.* **2011**, *133*, 17594−17597.
(20) Liu, G. L.; Long, Y.-T.; Choi, Y.; Kang, T.; Lee, L. P. *Nat. Methods* **2007**, *4*, 1015−1017.
(21) Haes, A. J.; Chang, L.; Klein, W. L.; Van Duyne, R. P. *J. Am. Chem. Soc.* **2005**, *127*, 2264−2271.
(22) Jun, Y.-W.; Sheikholeslami, S.; Hostetter, D. R.; Tajon, C.; Craik, C. S.; Alivisatos, A. P. *Proc. Natl. Acad. Sci. U. S. A.* **2009**, *106*, 17735−17740.
(23) Shi, L.; Jing, C.; Ma, W.; Li, D.-W.; Halls, J. E.; Marken, F.; Long, Y.-T. *Angew. Chem., Int. Ed.* **2013**, *52*, 6011−6014.
(24) Li, Y.; Jing, C.; Zhang, L.; Long, Y.-T. *Chem. Soc. Rev.* **2012**, *41*, 632−642.
(25) Alivisatos, P. *Nat. Biotechnol.* **2004**, *22*, 47−52.
(26) Xiong, B.; Zhou, R.; Hao, J.; Jia, Y.; He, Y.; Yeung, E. S. *Nat. Commun.* **2013**, *4*, 1−9.
(27) Boisselier, E.; Astruc, D. *Chem. Soc. Rev.* **2009**, *38*, 1759−1782.
(28) Bohren, C. F.; Huffman, D. R. *Absorption and Scattering of Light by Small Particles*; Wiley Interscience: New York, 1983.
(29) Maier, S. A. *Plasmonics: Fundamentals and Applications*; Springer-Verlag: New York, 2007.
(30) Guo, X.; Zhang, Q.; Sun, Y.; Zhao, Q.; Yang, J. *ACS Nano* **2012**, *6*, 1165−1175.
(31) Ge, B.; Lisdat, F. *Anal. Chim. Acta* **2002**, *454*, 53−64.
(32) von Wallbrunn, A.; Höltke, C.; Zühlsdorf, M.; Heindel, W.; Schäfers, M.; Bremer, C. *Eur. J. Nucl. Med. Mol. Imaging* **2007**, *34*, 745−754.
(33) Sun, Y.-X.; Zeng, X.; Meng, Q.-F.; Zhang, X.-Z.; Cheng, S.-X.; Zhuo, R.-X. *Biomaterials* **2008**, *29*, 4356−4365.
(34) Chen, Y.; Gibson, S. B. *Autophagy* **2008**, *4*, 246−248.
(35) Klimova, T.; Chandel, N. S. *Cell Death Differ.* **2008**, *15*, 660−666.

DOI: 10.1021/ja5112628
J. Am. Chem. Soc. 2015, 137, 1903−1908